Available online at www.sciencedirect.com
ScienceDirect
Trans. Nonferrous Met. Soc. China 33(2023) 2255−2271
Transactions of Nonferrous Metals Society of China
www.tnmsc.cn

Influence of homogenization treatment on microstructure and recrystallization behavior of 2195 Al−Li alloy

Rong FU[1], Yuan-chun HUANG[1,2,3], Yu LIU[3], Hui LI[1], Zhi-wen WANG[3]

1. School of Mechanical and Electrical Engineering, Central South University, Changsha 410083, China;
2. State Key Laboratory of High Performance and Complex Manufacturing, Central South University, Changsha 410083, China;
3. Research Institute of Light Alloy, Central South University, Changsha 410083, China

Received 12 March 2022; accepted 14 June 2022

Abstract: The microstructural evolution during homogenization treatment and the recrystallization behavior caused by Al_3Zr precipitate in 2195 alloy were investigated via scanning electron microscopy, X-ray diffraction, transmission electron microscopy and electron backscatter diffraction. The severe dendrite segregation in the as-cast alloy was removed during homogenization, but the process was limited by the slower dissolution of Al−Cu phases. Moreover, the Al_3Zr dispersoids precipitated in the sample homogenized by ramp heating rate of 30 °C/h (H30) were finer and denser compared to the samples subjected to other homogenization treatments (single-step, double-step, and ramp heating rate of 60 °C/h). The movement of dislocations and (sub)grain boundaries was resisted by the stronger Zener drag of finer and denser Al_3Zr dispersoids. Thus, a higher recrystallization resistance during the hot compression and subsequent solution treatment was achieved for H30 sample. This work can provide theoretical guidance for optimizing the heat treatment parameters of the as-cast 2195 Al alloy.

Key words: Al−Cu−Li alloy; homogenization; Al−Cu phase dissolution; Al_3Zr precipitate; recrystallization

1 Introduction

Al−Li alloys have attracted great attention in recent years due to their low density, high specific strength and modulus, good toughness, excellent corrosion resistance, and satisfactory fatigue resistance [1,2]. Several Al−Li alloys are widely used in aeronautics (e.g., upper or lower wing, empennage, and seat rails), astronautics (e.g., cryogenic tankage applications), and military areas [3−6]. It has been reported that addition of 1 wt.% Li (0.534 g/cm^3) into aluminum reduces the density by 3% and increases the elastic modulus by 6% [7]. Besides, it is commonly accepted that the comprehensive properties of Al−Li alloys can be effectively improved by adjusting the microstructure (such as the type, fraction, and density of precipitates) through regulating the concentrations of Cu and Li and adding other microalloying elements (such as Mg, Ag, Zr, Zn, and Mn) [8−10]. Nevertheless, dendritic segregation and coarse primary phases are formed during casting due to multi-trace elements and rapid solidification [11], resulting in an unfavorable influence on subsequent plastic deformation processes (such as extrusion, rolling, and forging) [12,13]. Meanwhile, many atoms are confined in the primary phase, thus reducing the precipitates during aging treatment. Therefore, a homogenization treatment is always carried out for casting ingots, which aims to remove micro-segregation, promote

Corresponding author: Yuan-chun HUANG, Tel: +86-13507315123, E-mail: ychuang@csu.edu.cn;
Yu LIU, Tel: +86-15273120641, E-mail: csuliuyu@csu.edu.cn
DOI: 10.1016/S1003-6326(23)66257-0

the uniform distribution of alloying elements, and increase the saturation of solute atoms in the Al matrix.

In the homogenization process for 2195 alloy, the eutectic phase is dissolved and Al_3Zr dispersoids are precipitated. The Al_3Zr dispersoids can effectively prevent the movement of dislocations and grain boundaries to inhibit recrystallization during hot working [14,15]. The effect of Al_3Zr dispersoids on recrystallization was previously found to be related to their size, distribution, and density, and controlled mainly by homogenization treatment [16,17]. For example, WANG et al [18] investigated the precipitation behavior of Al_3Zr dispersoids during different homogenization treatments and their influence on recrystallization for spray deposited 2195 alloy. DENG et al [19] revealed that more substructures are retained due to the formation of higher density and more uniform Al_3Zr dispersoids in double-step homogenization treatment for Al−Cu−Li−Zr alloys. LIU et al [20] achieved the strength and ductility improvement of 2195 alloys through two-step homogenization. GUO et al [21] proposed optimal double-step homogenization parameters to improve the uniformity of solute elements and the degree of recrystallization resistance for as-cast 2195 Al−Li alloy. To date, two-stage homogenization treatment is frequently employed to obtain fine and dense Al_3Zr precipitates. This method is based on a high driving force for nucleation induced by the low solubility of Zr in the aluminum matrix at the low-temperature stage and high diffusion rate to grow at the high-temperature stage.

It has been reported that ramp heating homogenization was carried out on 7xxx aluminum alloy, which achieved finer, denser, and more uniform Al_3Zr precipitates, resulting from higher supersaturation of Zr solutes and more heterogeneous nucleation sites on the second phase in the ramp heating stage [14,22,23]. Nevertheless, the study on the effects of ramp heating treatment on precipitates for 2195 Al−Cu−Li alloy is still limited. Therefore, in this work, the precipitation behavior of Al_3Zr dispersoids was studied under four different homogenization treatments, i.e., single-step, double-step, and ramp heating with heating rates of 30 and 60 °C/h. Their effect on recrystallization after hot compression followed by solution treatment was further investigated. The microstructural evolution of 2195 alloy during homogenization treatment was also studied. In particular, the dissolution process of the high melting point primary phase with different morphologies was systematically analyzed though microscopic characterization and kinetic analysis.

2 Experimental

The 2195 Al−Li alloy ingot used in this study was provided by Southwest Aluminum (Group) Co., Ltd., China. The chemical composition of the alloy was determined by inductively coupled plasma optical emission spectrometry (ICP–OES), and the results are shown in Table 1. Samples with dimensions of 15 mm × 8 mm × 15 mm were cut from the center of the as-cast plate and homogenized in a muffle furnace with a heating rate of 10 °C/min. The proper temperatures for single-step homogenization treatments were determined to be 515, 525, and 535 °C for 12−30 h near the dissolution temperature of Al_2Cu phases (530 °C) based on the DSC curve. Double-step homogenization treatments were performed at 470 °C for 8 h and 525 °C for 12−24 h, where the first step at 470 °C was selected to obtain fine Al_3Zr dispersoids and dissolve the eutectic phase with a low melting point. Ramp heating homogenization treatments were applied with heating rates of 30 and 60 °C/h up to the first step temperature. The detailed homogenization parameters for the as-cast 2195 alloy are listed in Table 2 and the corresponding samples are named as S515, S525, S535, D525, H30, and H60, respectively. The homogenized samples with dimensions of *d*8 mm × 12 mm were compressed by 60% in height using a Gleeble 3810 thermomechanical simulator at 470 °C and a strain rate of 0.1 s^{-1} to evaluate the recrystallization behavior, followed by solution treatment at 525 °C for 1 h. Figure 1 presents the schematic diagram for the whole experimental route.

The microstructure of all samples was observed by optical microscopy (OM, OLYMPOS-DSX500) and scanning electron microscopy (SEM, FEI-Phenom). The elemental distribution and the chemical composition of the phases were measured by energy dispersive spectrometry (EDS). The proportion of the primary phase was calculated by Image-Pro Plus software. The phase-type of the

Table 1 Chemical composition of 2195 Al−Li alloy (wt.%)

Cu	Li	Mg	Ag	Zr	Fe	Si	Ti	Zn	Mn	Al
3.98	0.99	0.32	0.32	0.12	0.082	0.037	0.034	0.0022	0.0016	Bal.

Table 2 Homogenization parameters for as-cast 2195 Al−Li alloy

Heat treatment	Treatment label	Parameter
Single-step homogenization	S515-12/18/24/30	515 °C; 12, 18, 24, 30 h
	S525-12/18/24/30	525 °C; 12, 18, 24, 30 h
	S535-12/18/24/30	535 °C; 12, 18, 24, 30 h
Double-step homogenization	D525-12/18/24	(470 °C, 8 h) + (525 °C, 12, 18, 24 h)
Ramp heating homogenization	H30	Heating at 30 °C/h to 470 °C and (470 °C, 8 h) + (525 °C, 24 h)
	H60	Heating at 60 °C/h to 470 °C and (470 °C, 8 h) + (525 °C, 24 h)

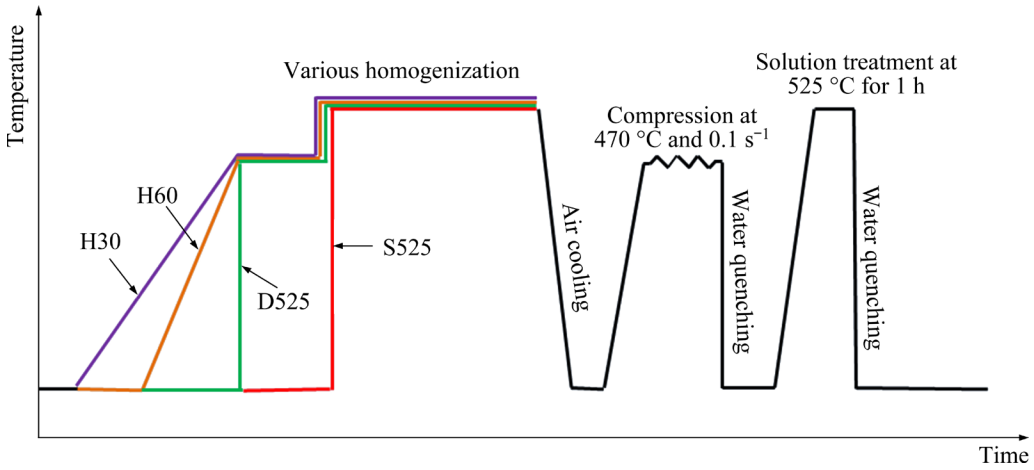

Fig. 1 Schematic diagram for whole experimental routes

samples was identified using the X-ray diffraction (XRD, X' Pert PRODSC) with a scanning speed of 5 (°)/min within the 2θ range of 10°−90°. The dissolution temperature of the primary phase was determined by differential scanning calorimetry (DSC, MDSCQ100) at a heating rate of 10 ℃/min from 100 to 605 ℃. The transmission electron microscopy (TEM, Talos F200X) was used to characterize the Al_3Zr dispersoids in the alloy during homogenization treatment. The TEM samples were mechanically ground to less than 80 μm and punched into 3 mm discs, and subsequently subjected to twin-jet polishing with the voltage of 15 V and temperature below −25 ℃ in an electrolyte solution containing 30 vol.% nitric acid and 70 vol.% methanol. Furthermore, the size distributions and average diameter of Al_3Zr dispersoids were determined by Image-Pro Plus software. The number density (N_v) of Al_3Zr was calculated using the equation: $N_v=N_0/(h+2b)$ [21], where N_0 refers to the number of dispersoids per unit area in the field of view, h is the thickness of TEM foil [19,24], and b represents the average radius of dispersoids. The specimens for electron backscatter diffraction (EBSD) measurement were sectioned parallel to the compression axis along the centerline and electropolished in a solution of 10 vol.% perchloric acid and 90 vol.% alcohol, and then observed by SEM equipped with an EBSD detector. The EBSD data were analyzed using HKL Channel 5 software.

3 Results

3.1 Microstructure of as-cast alloys

The OM image of the as-cast sample exhibits a typical dendritic structure, as shown in Fig. 2(a). The coarse phases composed of overlapping primary phases with different morphologies are distributed continuously at grain boundaries in Figs. 2(b−e). The coarse phases are divided into four parts in Fig. 2(c). Part A, with a smooth surface,

mainly contains Cu. It is difficult to distinguish the Al−Cu phase from the Al−Cu−Li phase because Li is too light to be detected by EDS. The B and C parts are obtained by the superposition of Al−Cu, Al−Cu−Mg, and enriched Mg−Ag phases. Part D mainly contains Al−Fe−Cu and Al−Cu phases.

The chemical compositions of the nine marked points in Figs. 2(d, e) are listed in Table 3. The molar ratio of the phases at Points 1, 2, and 7 is close to that of the Al_2Cu phase. The phases with honeycomb-like shapes at Points 3, 4, 8, and 9 are Al_2Cu phase with some Mg and Ag elements dissolved. Fewer Mg and Ag are dissolved in the gray area than those in the bright white area. The molar ratio at Point 5 is close to that of the Al_7Cu_2Fe phase, and Point 6 corresponds to Al_2CuMg phase attributed to a 1:1 molar ratio of Cu to Mg. In Fig. 2(e), the nanoneedle-shaped phases marked by the arrows in the enlarged view of a black dotted frame around the coarse phase are identified as T_1(Al_2CuLi) phase according to the morphology and distribution [25].

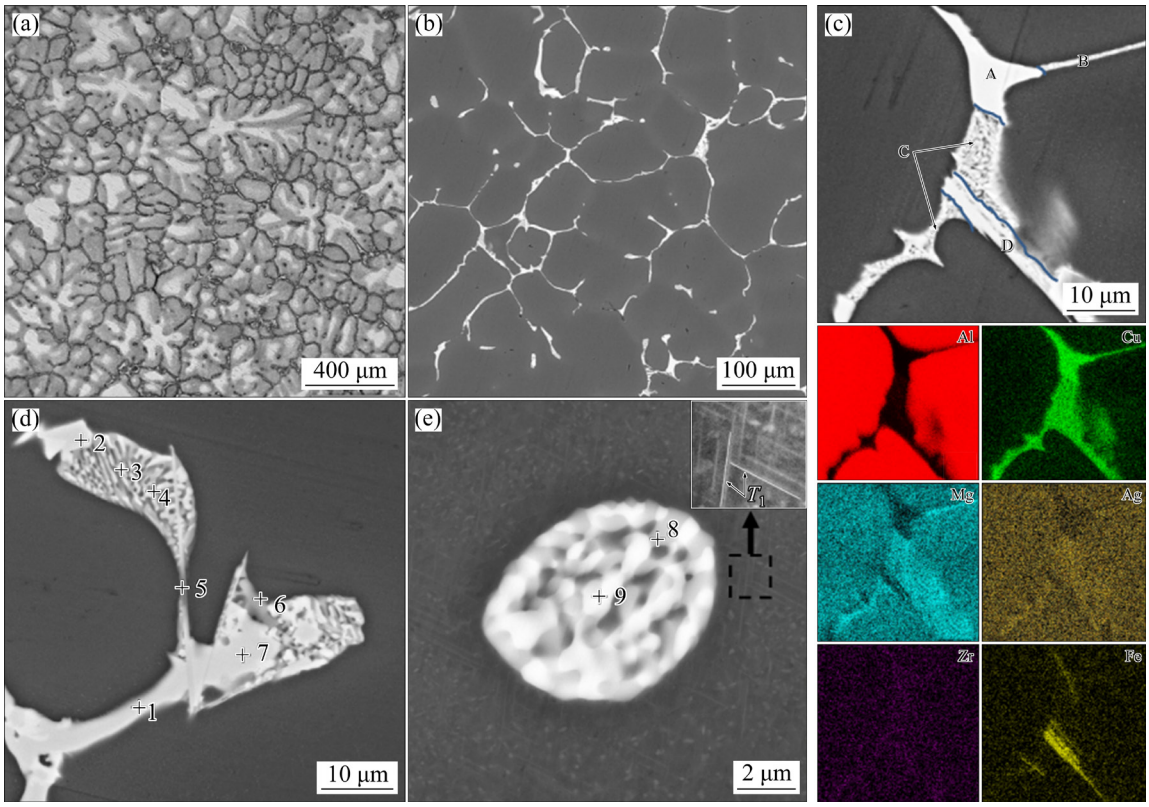

Fig. 2 Microstructures of as-cast 2195 Al−Li alloy: (a) OM image; (b, d, e) SEM images; (c) Corresponding EDS maps

Table 3 Chemical compositions of points in Figs. 2(d, e) (at.%)

Point No.	Al	Cu	Mg	Ag	Zr	Fe	Zn	Si	Ti	Mn	Close phase
1	69.82	29.63	0.40	−	−	−	0.04	0.06	0.01	0.03	Al_2Cu
2	65.57	31.83	2.08	0.15	0.11	0.04	0.02	0.18	−	0.01	Al_2Cu
3	73.44	21.42	4.08	0.85	−	0.02	0.02	0.12	0.04	0.01	Al_2Cu(Mg,Ag)
4	75.35	15.40	7.04	1.66	0.04	0.09	−	0.38	0.03	0.01	Al_2Cu(Mg,Ag)
5	70.91	23.79	0.17	0.02	−	4.98	−	0.07	−	0.04	Al_7Cu_2Fe
6	83.81	7.87	6.12	1.64	0.04	0.03	0.05	0.39	−	0.04	α(Al)+Al_2CuMg
7	68.65	30.46	0.63	−	0.08	0.03	−	0.15	−	−	Al_2Cu
8	61.69	25.95	6.36	5.67	0.12	−	−	0.20	0.01	−	Al_2Cu(Mg,Ag)
9	68.32	24.3	3.30	3.95	0.00	−	−	0.10	−	0.01	Al_2Cu(Mg,Ag)

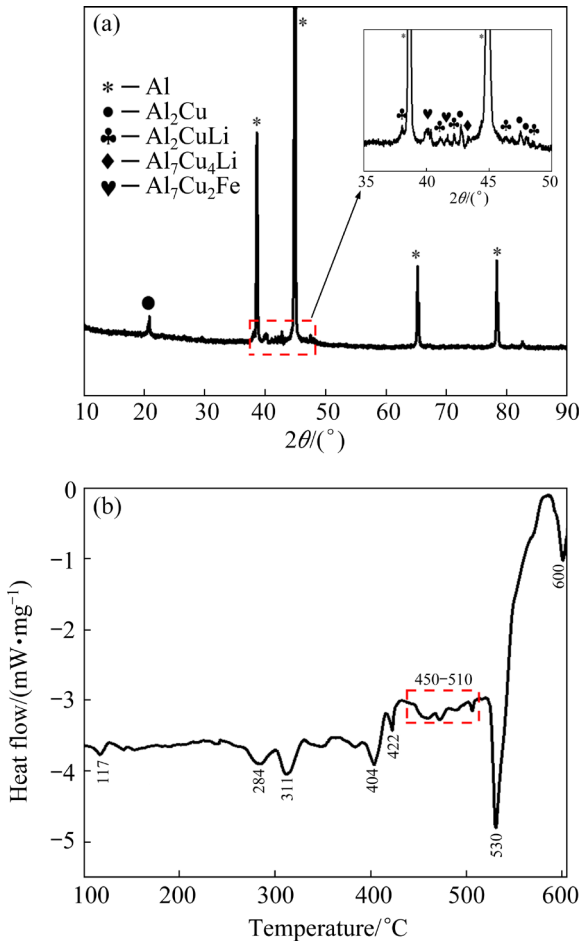

Fig. 3 XRD pattern (a) and DSC curve (b) of as-cast 2195 Al−Li alloy

Figure 3(a) shows the XRD pattern of the as-cast 2195 Al−Li alloy. Besides the characteristic peaks of the Al matrix, the characteristic peaks of Al_2Cu, Al_2CuLi, Al_7Cu_4Li, and Al_7Cu_2Fe phases can be observed. The DSC curve of the as-cast alloy is shown in Fig. 3(b). The endothermic peak at 117 °C is caused by the dissolution of the GP zone and the fine δ' (Al_3Li) phase [26]. The endothermic peaks at 280−430 °C are related to the dissolution of Al−Cu−Li phases with a low melting point, for instance, the peak at 284 °C corresponds to the T_1 phase, and the peak at 422 °C corresponds to the T_2 or T_B phases [26−28]. Many small endothermic peaks can be observed between 450 and 510 °C, which are mainly caused by Al_2CuMg and Mg−Ag phases [29,30]. Significant endothermic peaks at 530 and 600 °C are attributed to the dissolution of the Al_2Cu phase and the melting of the alloy, respectively. The above result shows that the upper-temperature limit of the homogenization treatment is 530 °C.

3.2 Microstructural evolution during homogenization

Figure 4 shows the microstructure of the 2195 Al−Li alloy after a single-step homogenization treatment. Almost all the dendritic structures are eliminated, and the grain size increases slightly with increase in temperature, as shown in Figs. 4(a−c). Finer second phases are distributed intermittently due to the high diffusion coefficient and long diffusion distance of atoms at a high temperature for a long time (Figs. 4(e−p)). The area fraction of the second phase decreases significantly compared with that of the as-cast alloy. The statistics data of the area fraction are given in Fig. 4(d). There are apparent overburning structures (remelting zones of the compounds) marked by red arrows at the grain boundaries at 535 °C, such as overheating triangle sections and re-melting balls [31], as shown in Figs. 4(m−p).

The EDS element distribution diagram of the sample after the first step in double-step homogenization treatment is given in Fig. 5(a). Compared with the EDS image of the as-cast alloy (Fig. 2(c)), the segregation of Mg and Ag elements is eliminated, and some Cu and Fe elements are left at the grain boundaries. Figures 5(b−e) show that the coarse phases are gradually fractured and spheroidized with the increase in homogenization time. At the same time, there is almost no change in the needle-like phase. Based on the chemical composition of the nine points in Table 4, it is speculated that the main residual phases may be Al_2Cu and Al_7Cu_2Fe.

Figure 6 present the XRD patterns of the homogenized 2195 Al−Li alloy. The characteristic peaks corresponding to Al_2Cu, Al_2CuLi, and Al_7Cu_4Li phases are gradually weakened and disappear with the increase in temperature, but the weaker characteristic peak of Al_7Cu_2Fe still exists. The characteristic peaks of the aluminum matrix are shifted slightly (see illustration in Figs. 6(a, b)), which is probably due to the solid solution of solute atoms (such as Cu, Mg, Li, and Ag). It can be seen from the DSC curves in Fig. 7(a) that the endothermic peak of the eutectic phase with the low melting point disappears during the first step of homogenization treatment, but the characteristic peak near 530 °C does not change much. The enlarged view of the DSC curve in Fig. 7(b) shows that the peak near 530 °C disappears after the single-step or double-step homogenization treatment.

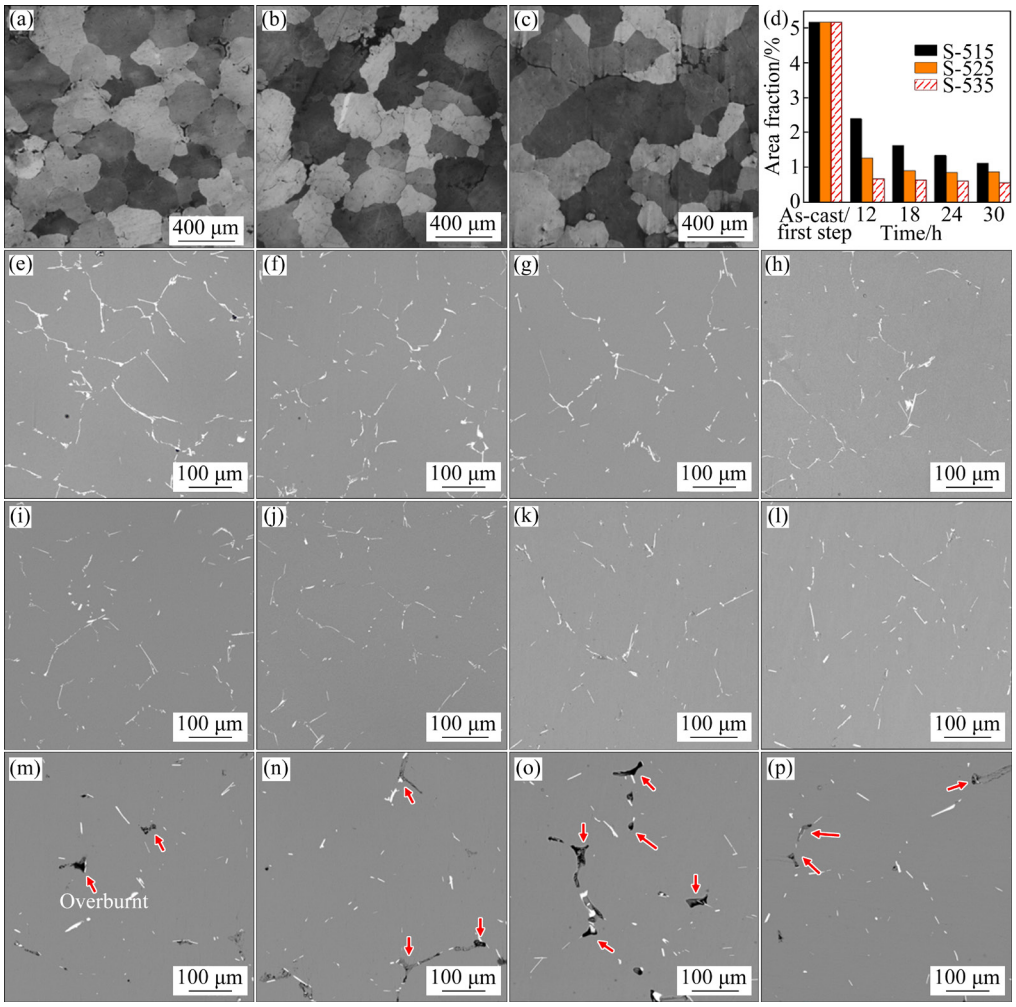

Fig. 4 Microstructures of 2195 Al−Li alloy after single-step homogenization treatment: (a−c) OM images at 515, 525, and 535 ℃ for 24 h, respectively; (d) Statistical result of area fraction of second phase; (e−h) SEM images at 515 ℃ for 12, 18, 24, 30 h, respectively; (i−l) SEM images at 525 ℃ for 12, 18, 24, and 30 h, respectively; (m−p) SEM images at 535 ℃ for 12, 18, 24, 30 h, respectively

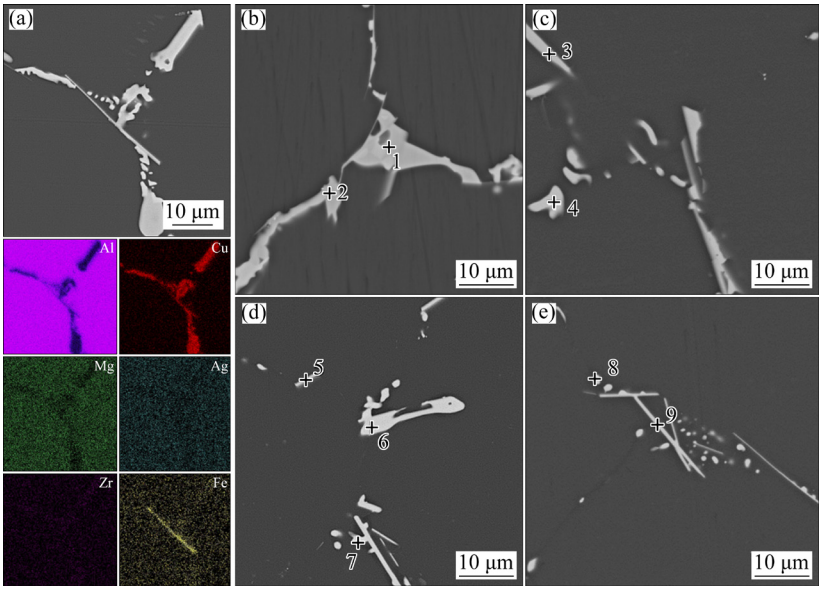

Fig. 5 SEM images of 2195 Al−Li alloy homogenized under different conditions: (a, b) 470 ℃, 8 h; (c−e) (470 ℃, 8 h) + (525 ℃, 12, 18, 24 h)

Table 4 Chemical compositions of points in Figs. 5(b−e) (at.%)

Point No.	Al	Cu	Mg	Ag	Zr	Fe	Zn	Si	Ti	Mn	Close phase
1	64.54	32.04	0.79	0.16	0.26	1.98	0.09	0.12	0.02	0.01	Al_2Cu
2	73.77	18.61	0.10	0.034	−	6.95	0.07	0.16	−	−	α(Al)+Al_7Cu_2Fe
3	77.08	16.28	0.21	0.00	0.00	6.38	−	−	0.04	0.01	α(Al)+Al_7Cu_2Fe
4	66.76	31.90	0.88	0.06	0.29	0.05	−	0.05	−	−	Al_2Cu
5	90.68	6.50	0.42	0.06	0.02	2.23	−	−	−	0.10	α(Al)+Al_7Cu_2Fe
6	74.74	18.04	0.07	−	0.04	7.06	−	0.02	0.02	−	α(Al)+Al_7Cu_2Fe
7	79.07	19.49	0.64	0.07	0.54	0.07	0.03	0.01	0.04	0.03	α(Al)+Al_2Cu
8	81.13	17.70	0.71	0.06	0.33	0.02	−	0.02	−	0.03	α(Al)+Al_2Cu
9	85.59	10.40	0.27	0.03	0.03	3.64	−	−	−	0.04	α(Al)+Al_7Cu_2Fe

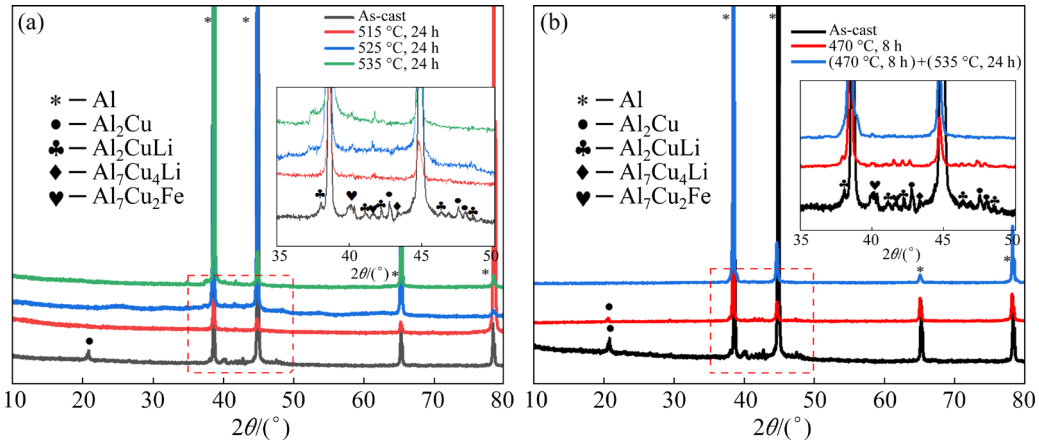

Fig. 6 XRD patterns of 2195 Al−Li alloy after single-step (a) and double-step (b) homogenization treatment

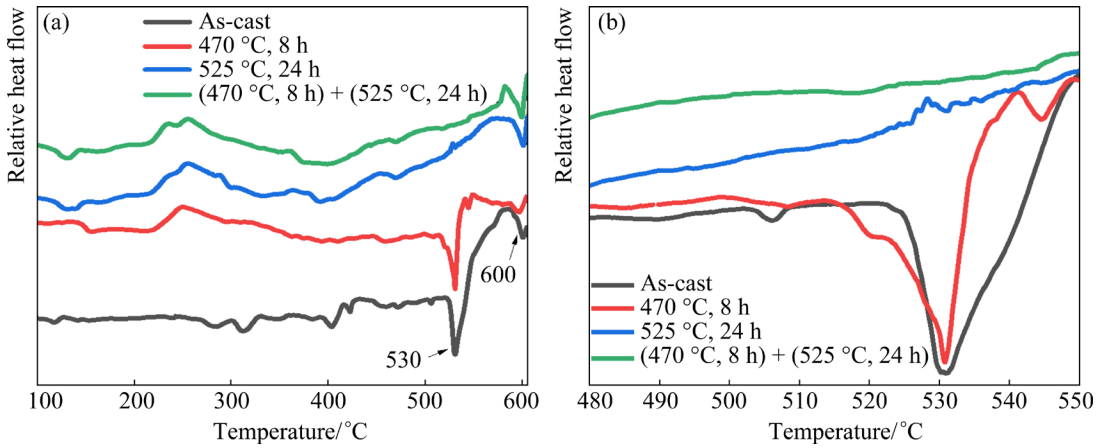

Fig. 7 DSC curves at 100−600 °C (a) and their enlarged curves at 480−550 °C (b) of 2195 Al−Li alloy after homogenization treatment

The dispersed nanoscale Al_3Zr particles are precipitated during homogenization treatment, and the characteristics of the dispersoids are displayed in Fig. 8. It can be found that the dispersoids have a regular spherical shape, but their uniformity, size, and number density in different homogenized alloys vary. The difference is related to the driving force for nucleation (supersaturation of solid solution) and coarsening (diffusivity of Zr atoms) of the Al_3Zr dispersoids [32]. Compared with other homogenization conditions, the location distribution of the Al_3Zr dispersoids within the matrix is more

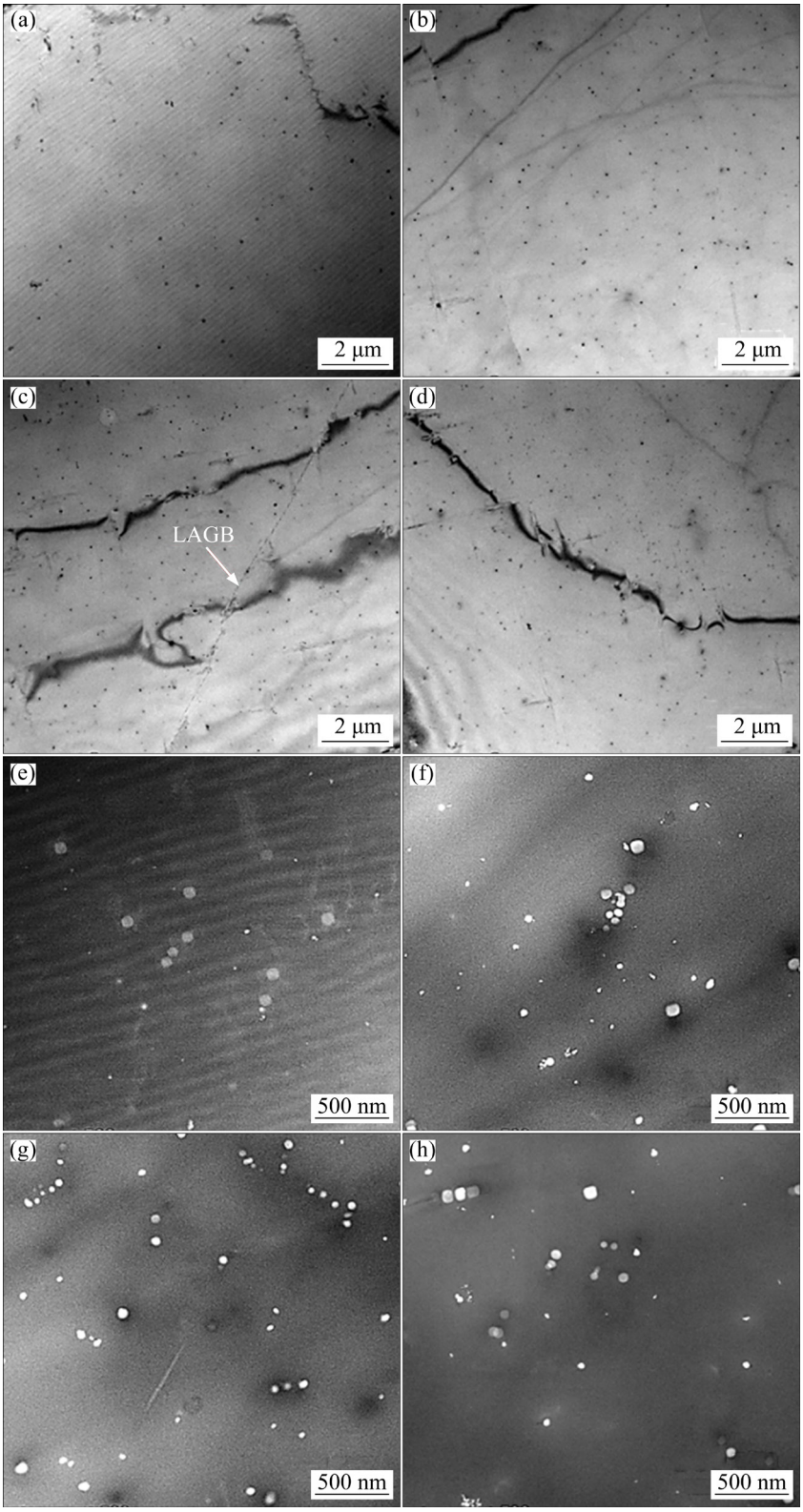

Fig. 8 STEM and dark field images of homogenized 2195 Al−Li alloys: (a, e) S525-24; (b, f) D525-24; (c, g) H30; (d, h) H60

homogeneous in H30 sample, as can be seen from Figs. 8(e−h). The size distribution of Al_3Zr dispersoids is shown in Fig. 9(a). It can be seen that Al_3Zr precipitates of H30 have the narrowest range of diameter, and the maximum size is smaller than that of the other three homogenized samples. The average diameters and number densities of Al_3Zr dispersoids under S525-24, D525-24, H30, and H60

conditions are determined to be 69, 47, 39, and 45 nm and 17, 27, 44, and 31 μm^{-3}, respectively, as shown in Fig. 9(b). This indicates that finer and denser Al_3Zr particles are precipitated in H30. The selected area electron diffraction (SAED) patterns of D525-24 and H30 viewed along the $[100]_{Al}$ and $[112]_{Al}$ directions are presented in Figs. 10(a, b), respectively. The two types of diffraction spots are correlated with Al matrix and $L1_2$-structured Al_3Zr phase, respectively, and the diffraction spots of the Al_3Zr phase marked by red arrows are found at the positions of 1/2 $[220]_{Al}$ [20,32]. Moreover, the EDS mapping in Figs. 10(c, d) shows that Zr element is gathered in the spherical particles, while other elements (Cu and Mg) are evenly distributed.

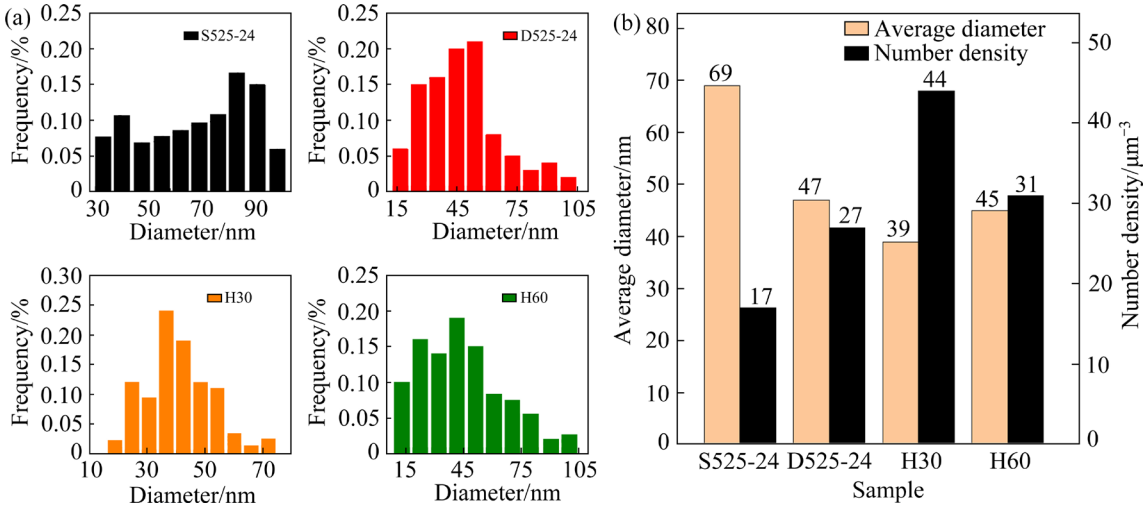

Fig. 9 Size distributions (a) and average diameters and number densities (b) of Al_3Zr dispersoids

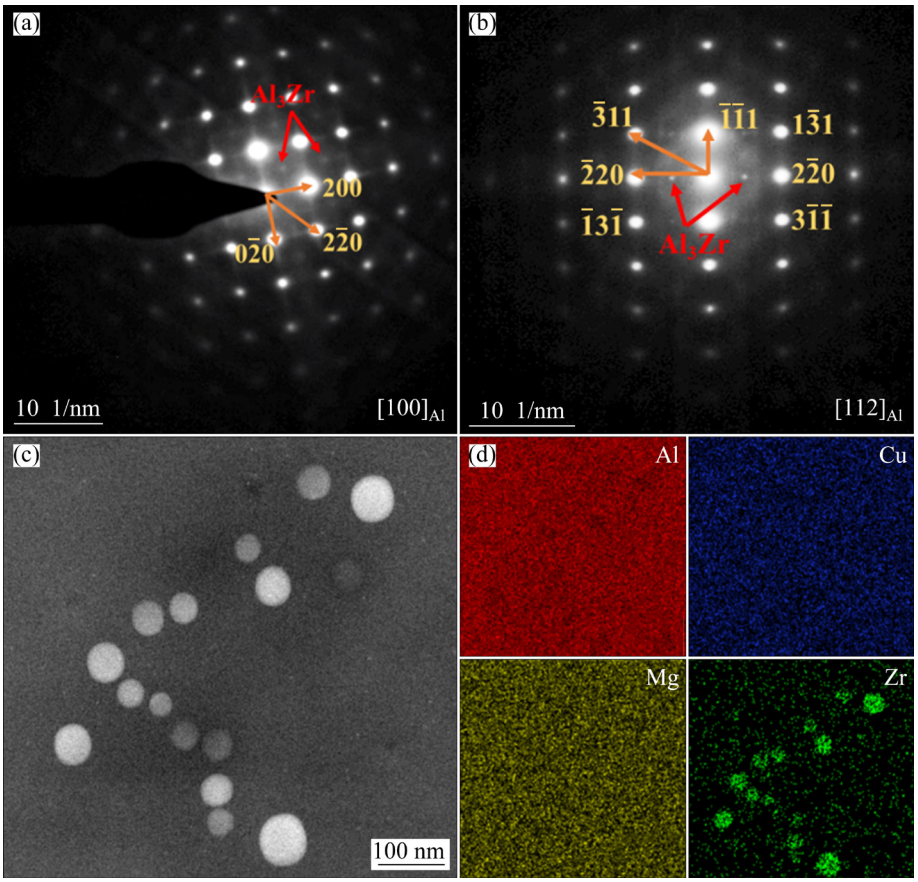

Fig. 10 SAED patterns viewed along $[100]_{Al}$ of D525-24 (a) and $[112]_{Al}$ of H30 (b) zone axes, and HAADF-STEM image (c) and EDS mapping (d) of dispersoids in H30

3.3 Recrystallization behavior after different homogenization treatments

To clarify the effect of Al_3Zr dispersoids on the recrystallization behaviors, EBSD test was performed on the hot compressed alloys, and the results are shown in Fig. 11. It can be seen that the grains are shortened in the thickness direction and elongated in the width direction. The inverse pole figure (IPF) maps in Figs. 11(a−d) indicate crystal orientations of grains by different colors. The boundaries with the misorientation angles of 2°−15° are defined as low angle grain boundaries (LAGB) marked with white lines, and the black lines represent high angle grain boundaries (HAGB) with the misorientation angle above 15°. The corresponding grain boundary misorientation distributions are shown in Figs. 11(e−h). It is found that the frequency of LAGBs in H30 is greater than that in S525-24, D525-24, and H60, but the difference between them is small. Furthermore, the accounted frequency of LAGBs at 2°−5° presents the same trend. The corresponding recrystallization maps in Figs. 11(i−l) show the recrystallized microstructures. The mean misorientation angle within grains above 1° can be regarded as a deformed structure (highlighted with red areas); while the substructure highlighted with yellow areas corresponds to the grain with internal misorientation angle below 1° and the misorientation angle between subgrains above 1°. The rest of the areas highlighted with blue color represent recrystallized microstructure with a lower strain level [33]. The recrystallization fractions of samples treated with different homogenization treatments are calculated to be 1.98%, 1.84%, 1.40%, and 1.51%, respectively. Due to the resistance of Al_3Zr dispersoids and compression within a short time, recrystallization (DRX) behavior rarely occurs in the compression process.

The EBSD images of the hot compressed samples after solution treatment at 525 ℃ for 1 h are shown in Fig. 12. Compared with the samples before solution treatment in Fig. 11, it can be seen that the frequency of LAGBs decreases, especially in S525-24 and D525-24. Moreover, the decreased fraction of the LAGBs at 2°−5° under H30 and H60 conditions is less than that of the other two homogenization conditions, which indicates that the recovery is strongly restrained. The proportions of corresponding recrystallized microstructures are shown in Figs. 12(i−l). It can be found that the recrystallization fraction in S525-24 and D525-24 increases significantly from 1.98% and 1.84% to 15.2% and 11.6%, respectively. The phenomenon is mainly due to the thermal activation energy provided in solution treatment and the insufficient

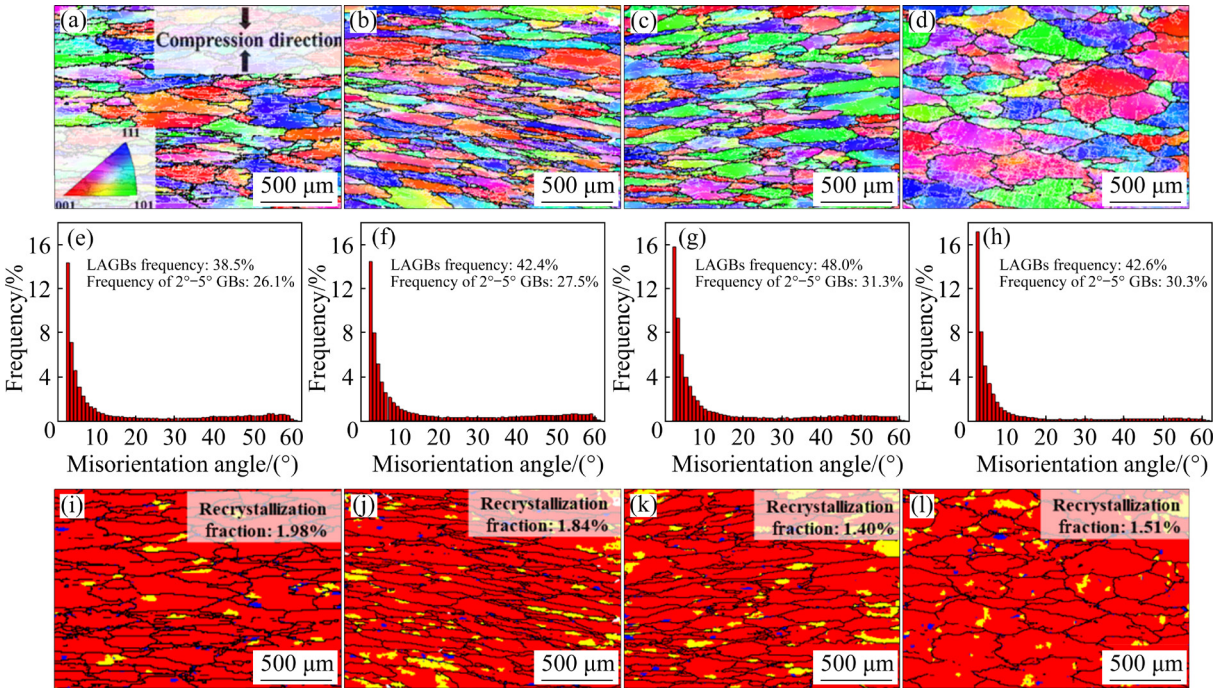

Fig. 11 IPF maps (a−d), grain boundary misorientation distributions (e−h), and corresponding recrystallization maps (i−l) of S525-24, D525-24, H30, and H60 after hot compression, respectively

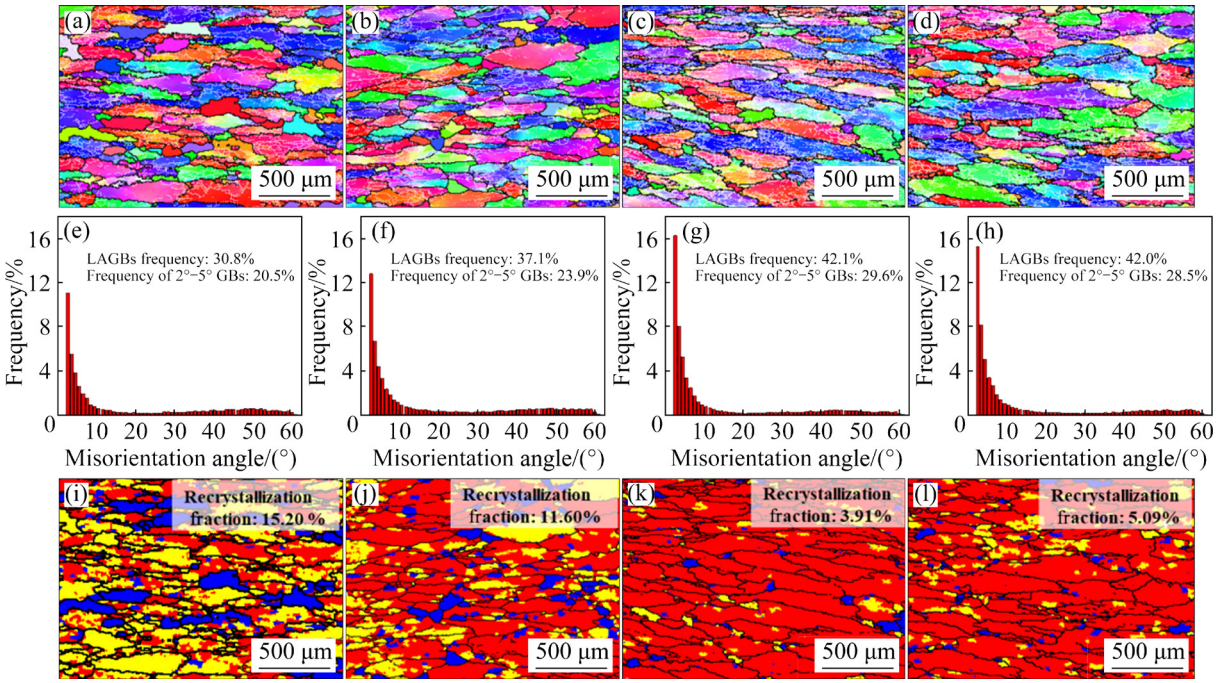

Fig. 12 IPF maps (a−d), grain boundary misorientation distributions (e−h), and corresponding recrystallization maps (i−l) of S525-24, D525-24, H30, and H60 treated by hot compression after solution treatment at 525 ℃ for 1 h, respectively

pinning force from coarser and fewer Al_3Zr dispersoids for the movement of the dislocations and (sub)grain boundaries. However, there is a slight increase in the recrystallized fraction of H30 after solution treatment, resulting from the stronger inhibition caused by finer and denser Al_3Zr dispersoids for recrystallization behavior. In addition, it is confirmed that Al_3Zr dispersoids exhibit good thermal stability even at higher temperatures.

4 Discussion

4.1 Dissolution of primary phases with different morphologies

During the homogenization treatment, the dissolution of the secondary phase is commonly divided into intragranular and intergranular processes. Here, the dissolution time of the tiny phase was not considered, as the dissolution rate of the tiny phase within the grain is much faster than that of the coarse phase at the grain boundary. As previously reported, understanding the dissolution process of the primary phase with a high melting point is beneficial to achieving effective homogenization [12]. Hence, this work focused on the dissolution process of the Al−Cu phase. Furthermore, the dissolution rate is also influenced by the shape of the phases [34]. The above microstructure characterization indicates that the morphology of the Al−Cu phases changes from plate-like to spherical shape in the dissolution process, as schematically shown in Fig. 13(a). Accordingly, the dissolution rate also changes. Based on Fick's law of diffusion and the model for dissolution kinetics of the secondary phase proposed by WHELAN [35], the dissolution of Al−Cu phases with different morphologies at grain boundaries was discussed.

4.1.1 Dissolution of plate-like phase

The essence of dissolution is atomic diffusion, which can be described by Fick's second law. And the diffusion coefficient (D) conforms to the Arrhenius equation as follows:

$$D = D_0 \exp[-Q/(RT)] \quad (1)$$

where D_0 is the diffusion constant; Q is the diffusion activation energy; R is the molar gas constant (8.314 J/(mol·K)); T is the thermodynamic temperature. The diffusion coefficient of Cu is smaller than that of Mg, Ag, and Zr elements. The parameters of Cu in aluminum are D_0(Cu)=0.084 cm^2/s and

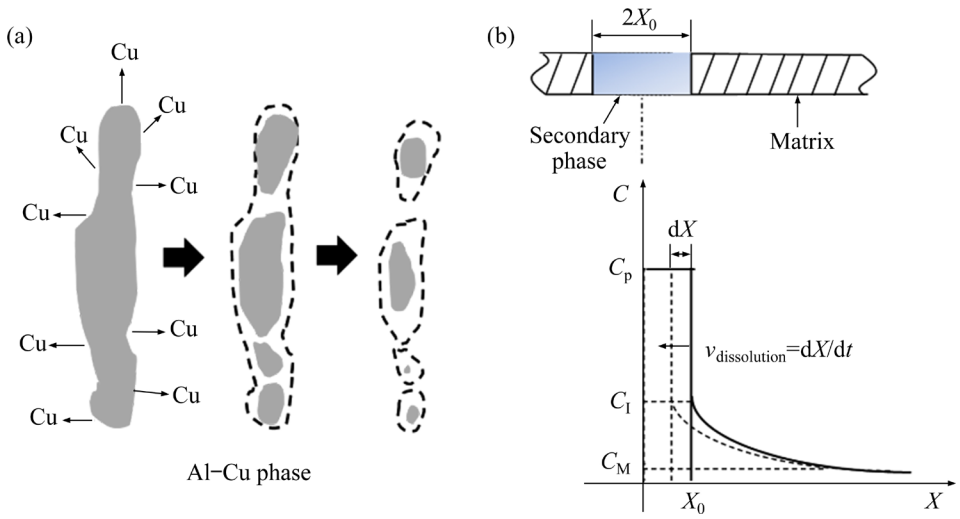

Fig. 13 Schematic diagrams of dissolution process for Al−Cu phase (a) and solute concentration distribution between plate-like phase and Al matrix (b)

Q(Cu)=136.8 kJ/mol [36].

The schematic diagram of the solute concentration distribution is shown in Fig. 13(b), assuming that the diffusion and dissolution of the network/plate-like phase at the grain boundaries occur in a semi-infinite space. In Fig. 13(b), X is the half-thickness of the plate-like shape, X_0 is the half-thickness of the initial phase, x is the diffusion distance, C_p and C_M are the solute concentrations in the primary phase and matrix, respectively, and C_I is the solute concentration at the interface between the primary phase and the matrix. According to Fig. 13(b), the initial and boundary conditions of concentration are as follows:

$$\begin{cases} C(x,t=0)=C_M \\ C(X,t)=C_I \end{cases} (x>X) \tag{2}$$

where t is the diffusion time.

According to Fick's second law and Eq. (2), the distribution curve of the solute concentration in the diffusion process is expressed by the error function solution of Fick's second law as follows:

$$C(x,t)=C_I-(C_I-C_M)\cdot\mathrm{erf}\frac{(x-X)}{2\sqrt{Dt}} \tag{3}$$

Based on Eq. (3) and the solute flux at the secondary phase/matrix interface maintaining equilibrium [37], the evolution equation of the thickness of the plate-like phase with diffusion time is as follows:

$$\frac{X}{X_0}=1-\frac{K}{X_0}\sqrt{\frac{Dt}{\pi}} \tag{4}$$

where K is a concentration parameter, which can be expressed as K=2(C_I−C_M)/(C_p−C_I), where $C_p \gg C_I$, C_M. It has been reported that the value of K is less than 0.3 for most alloy systems, and K=0.1 is quite typical [38]. WHELAN [35] suggested that 0.01 is a suitable value for K to predict the dissolution of the plate-like second phase θ in Al−Cu alloy. WANG et al [18] and GUO et al [21] determined that the value of K should be selected as 0.05 to accurately calculate the dissolution of the Al−Cu phase in 2195 Al alloy. In addition, the analysis results agree with the in-situ SEM observation. Thus, the K value for dissolution of the Al−Cu phase of 2195 alloy in this study is taken as 0.05.

4.1.2 Dissolution of spherical phase

The initial and boundary conditions of the spherical phase are the same as those of the plate-like phase. The distribution curve of the solute concentration is obtained as follows:

$$C(r,t)=C_I-(C_I-C_M)\frac{R_1}{r}\cdot\mathrm{erf}\frac{(r-R_1)}{2\sqrt{Dt}} \tag{5}$$

where R_1 is the radius of the phase, and r is the diffusion distance of the solute atom. The evolution equation of the radius of the spherical phase with diffusion time is expressed as

$$\frac{R_1}{R_0}=1-\frac{KDt}{2R_0^2}-\frac{K}{R_0}\sqrt{\frac{Dt}{\pi}} \tag{6}$$

where R_0 is the radius of the initial spherical phase.

The dissolution rate of the spherical phase is

much faster than that of the plate-like phase under the same conditions. The half-thickness in most of the second phase of as-cast 2195 Al−Li alloy at grain boundary is less than 30 μm (Fig. 2). The dissolution curves of plate-like and spherical phases with sizes of 1−30 μm at 525 °C are shown in Fig. 14. It is seen that the dissolution time of the spherical and plate-like phases with the same size (8 μm) is less than 1 h and greater than 70 h, respectively. The dissolution process of the Al−Cu phase includes both the dissolution of the plate-like phase and the spherical phase. Hence, the dissolution time is between that of the entirely spherical phase and the plate-like phase.

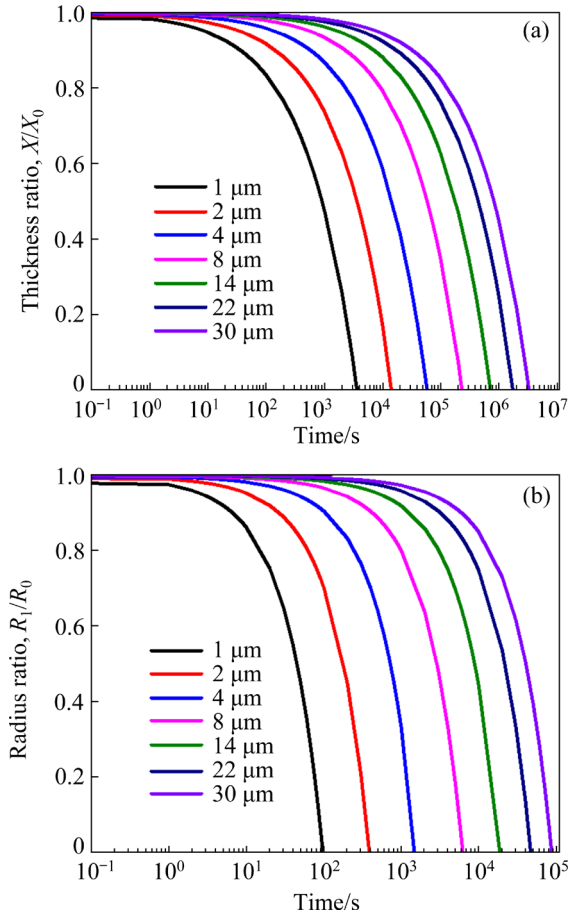

Fig. 14 Dissolution rate curves of plate-like phase (a) and spherical phase (b) at grain boundaries

4.2 Precipitation behavior of Al_3Zr dispersoids

The above experimental results demonstrate that the differences in number density and diameter of Al_3Zr dispersoids are related to the homogenization treatment condition. In general, the precipitation process of dispersoids includes three stages: nucleation, growth, and coarsening; where nucleation has a critical influence on the number density and distribution of the dispersed phase [39]. Previous studies have reported that the nucleation of the Al_3Zr phase mainly depends on the supersaturation of Zr atoms in the Al matrix [20,40]. It is confirmed that a stronger driving force for the nucleation of Al_3Zr dispersoids is provided by the higher supersaturation of the solid solution at a lower temperature. The critical nucleation radius is negatively correlated with the undercooling. Therefore, the number density of Al_3Zr dispersoids in S525-24 is lower than that in the other three homogenized samples due to the insufficient driving force for nucleation at the higher initial temperature. Similarly, the samples treated by ramp heating homogenization can yield a larger number of Al_3Zr dispersoids due to the higher supersaturation at a lower temperature for a long time in the ramp heating process.

Theoretically, the minimum activation energy barrier of heterogeneous nucleation at dislocations and high-angle boundaries is less than that of homogeneous nucleation in the matrix [41−43]. Since dislocations are absent in the samples during homogenization treatment, the interface between the second phase and the matrix is the preferred site for precipitation. Numerous sites for precipitation are provided in the ramp heating process, while most of the second phases with low melting points dissolve at the initial high temperature during the single-step and double-step homogenization. These mechanisms of heterogeneous precipitation at the second phase have also been reported in previous studies [14,44].

In addition, the higher the temperature, the higher the diffusion rate of atoms. The diffusion coefficient D of Zr atoms is estimated by Eq. (1) (where D_0=7.28×10^{-2} m^2/s, and Q=242 kJ/mol). The diffusion rate at 470 °C (7.05×10^{-19} m^2/s) is slower than that at 525 °C (1.05×10^{-17} m^2/s) [45]. This means that the growth of the Al_3Zr dispersoids is fast due to the rapid diffusion rate at the higher temperature, resulting in the larger diameter dispersoids in S525-24. In contrast, the coarsening of particles for H30 sample in the high temperature stage is limited by the large consumption of Zr atoms in the initial stage and the lower supersaturation [46,47]. Hence, finer and denser Al_3Zr dispersoids can be obtained by the ramp

heating homogenization treatment with a slow heating rate.

4.3 Effect of Al_3Zr particles on recrystallization resistance

It is believed that the inhibition of recrystallization is beneficial to the mechanical properties and corrosion resistance of aluminum alloys. Recrystallization can be defined as forming new strain-free grains by migrating high angle grain boundaries in a deformed microstructure [48,49]. Typically, the strain energy stored in the form of subgrain boundaries from the hot compression process is used as the driving force to induce recrystallization in the subsequent solution treatment [17]. Nevertheless, the recrystallization process is hindered by pinning the rearrangement of dislocations and the movement of grain boundary resulting from fine particles. It is widely accepted that the effect of fine precipitates on the nucleation stage of recrystallization is more important than that on the growth stage [50]. The recrystallized grain will be obtained if the grain nucleus grows up to the critical radius of nucleation (R_C). R_C can be calculated by the following Gibbs–Thompson formula [21]:

$$R_C = \frac{4\gamma_{GB}}{P_D - P_Z} \tag{7}$$

where γ_{GB} represents the specific grain boundary energy, approximately (0.3 J/m^2), and the stored energy P_D remains consistent in this study due to the same deformation conditions for all samples. Consequently, the valid driving force (P_D−P_Z) mainly depends on the Zener drag force P_Z of Al_3Zr dispersoids (i.e., the pinning pressure of dispersoids on the dislocation and subgrain boundaries) for recrystallization. The Zener drag force is calculated by the following relationship [21]:

$$P_Z = \frac{3 f_v \gamma_{GB}}{2 r_1} \tag{8}$$

where r_1 and f_v are the mean radius and volume fraction of the dispersoids, respectively. The ratio of f_v to r_1 determines the Zener pinning pressure based on Eq. (8). It can be seen that the smaller diameter and larger volume fraction of fine particles result in a higher value of P_Z. Compared with S525, D525, and H60 samples, a higher value of P_Z is obtained in H30 sample due to the finer and denser Al_3Zr dispersoids. This indicates that the nucleus of recrystallization is not readily obtained due to a large R_C in H30 sample. Moreover, the Al_3Zr dispersoids with favorable thermal stability do not dissolve into the matrix and still play an effective role in impeding the recovery and recrystallization at high temperatures. Thus, the recrystallization fraction of H30 sample is smaller compared to that under other homogenization conditions in the hot compression process and the subsequent solution treatment, which is consistent with the results of EBSD in Figs. 11 and 12.

5 Conclusions

(1) Most of the segregation of atoms and coarse eutectic phase at grain boundary was eliminated in the as-cast 2195 Al−Li alloy during homogenization, while the Fe-rich phases were barely dissolved into the matrix. The Al−Cu phases changed from plate-like to spherical shape during dissolution. The dissolution rate was relatively slow due to the lower diffusion rate of Cu atoms, which played a deciding role in the homogenization process.

(2) Compared with the samples treated by the single-step, double-step, and ramp heating with rapid heating rate (60 ℃/h) homogenization treatments, smaller diameter (D_{ave}=39 nm) and higher density (N_V=44 μm^{-3}) dispersoids of the $L1_2$-structured Al_3Zr phase were precipitated in the homogenized sample with a ramp heating rate of 30 ℃/h (H30). This was mainly due to the stronger driving force for the nucleation and the slower growth of dispersoids at a lower temperature in the ramp heating stage.

(3) The precipitation of Al_3Zr dispersoids effectively pinned the movement of the dislocations and (sub)grain boundaries to hinder the recrystallization process during the hot compression and the subsequent solution treatment. A stronger pinning force was provided due to the finer and denser Al_3Zr dispersoids in the H30 sample, leading to a lower recrystallization fraction compared with the other three homogenization treatments. Based on the above analysis, the homogenization treatment with a ramp heating rate of 30 ℃/h was confirmed to be suitable for as-cast 2195 Al−Li alloys.

Acknowledgments

The authors are grateful for the financial support from the National Natural Science Foundation of China (No. U1837207).

References

[1] WANG Xiao-ya, JIANG Jian-tang, LI Guo-ai, WANG Xiao-ming, SUN Jian, ZHEN Liang. Effects of coarse Al_2CuLi phase on the hot deformation behavior of Al−Li alloy [J]. Journal of Alloys and Compounds, 2020, 815: 152469.

[2] LI Qun, NING Jian, CHEN Lei, HU Jian-liang, LIU Yuan-xi. The mechanical response and microstructural evolution of 2195 Al−Li alloy during hot tensile deformation [J]. Journal of Alloys and Compounds, 2020, 848: 156515.

[3] RIOJA R J, LIU J. The evolution of Al−Li base products for aerospace and space applications [J]. Metallurgical and Materials Transactions A, 2012, 43: 3325−3337.

[4] EL-ATY A A, XU Yong, ZHANG Shi-hong, MA Yan, CHEN Da-yong. Experimental investigation of tensile properties and anisotropy of 1420, 8090 and 2060 Al−Li alloys sheet undergoing different strain rates and fibre orientation: A comparative study [J]. Procedia Engineering, 2017, 207: 13−18.

[5] EL-ATY A A, XU Yong, GUO Xun-zhong, ZHANG Shi-hong, MA Yan, CHEN Da-yong. Strengthening mechanisms, deformation behavior, and anisotropic mechanical properties of Al−Li alloys: A review [J]. Journal of Advanced Research, 2018, 10: 49−67.

[6] ZHANG Cun-sheng, LIU Ming-fu, MENG Zi-jie, ZHANG Qing-you, ZHAO Guo-qun, CHEN Liang, ZHANG Hao, WANG Jia. Microstructure evolution and precipitation characteristics of spray-formed and subsequently extruded 2195 Al−Li alloy plate during solution and aging process [J]. Journal of Materials Processing Technology, 2020, 283: 116718.

[7] GAO Zhen, CHEN Jiang-hua, DUAN Shi-yun, YANG Xiu-bo, WU Cui-lan. Complex precipitation sequences of Al−Cu−Li−(Mg) alloys characterized in relation to thermal ageing processes [J]. Acta Metallurgica Sinica (English Letters), 2016, 29: 94−103.

[8] XIONG Chun, JIANG Mang, XU Jin-jun. Effects of homogenization process on precipitation of Al_3Zr and recrystallization resistance in Al−Cu−Li−Zr alloy [J]. IOP Conference Series: Earth and Environmental Science, 2018, 186: 012051.

[9] NING Hong, LI Jin-feng, MA Peng-cheng, CHEN Yong-lai, ZHANG Xu-hu, ZHANG Kai, ZHANG Rui-feng. Evolution of aging precipitates in an Al−Li alloy with 1.5 wt.% Li concentration [J]. Vacuum, 2020, 182: 109677.

[10] GUMBMANN E, GEUSER F D, SIGLI C, DESCHAMPS A. Influence of Mg, Ag and Zn minor solute additions on the precipitation kinetics and strengthening of an Al−Cu−Li alloy [J]. Acta Materialia, 2017, 133: 172−185.

[11] MA Xiao-ping, LI Dian-zhong. Non-equilibrium solidification and microsegregation mechanism based on interface evolution and discrete crystal growth [J]. Metallurgical and Materials Transactions A, 2015, 46: 549−555.

[12] DENG Ying, YIN Zhi-min, CONG Fu-guan. Intermetallic phase evolution of 7050 aluminum alloy during homogenization [J]. Intermetallics, 2012, 26: 114−121.

[13] JIA P F, CAO Y H, GENG Y D, HE L Z, XIAO N, CUI J Z. Effects of D.C. current on the phase transformation in 7050 alloy during homogenization[J]. Materials Characterization, 2014, 96: 21−27.

[14] WU H, WEN S P, HUANG H, LI B L, WU X L, GAO K Y, WANG W, NIE Z R. Effects of homogenization on precipitation of $Al_3(Er,Zr)$ particles and recrystallization behavior in a new type Al−Zn−Mg−Er−Zr alloy [J]. Materials Science and Engineering: A, 2017, 689: 313−322.

[15] XIAO Hong-yu, LI Yu-gang, GENG Ji-wei, LI Hong-ping, WANG Ming-liang, CHEN Dong, LI Zhu-guo, WANG Hao-wei. Effects of nano-sized TiB_2 particles and Al_3Zr dispersoids on microstructure and mechanical properties of Al−Zn−Mg−Cu based materials [J]. Transactions of Nonferrous Metals Society of China, 2021, 31: 2189−2207.

[16] ROBSON J D. A new model for prediction of dispersoid precipitation in aluminium alloys containing zirconium and scandium [J]. Acta Materialia, 2004, 52: 1409−1421.

[17] TSIVOULAS D, PRANGNELL P B. The effect of Mn and Zr dispersoid-forming additions on recrystallization resistance in Al−Cu−Li AA2198 sheet [J]. Acta Materialia, 2014, 77: 1−16.

[18] WANG Yong-xiao, MA Xin-wu, ZHAO Guo-qun, XU Xiao, CHEN Xiao-xue, ZHANG Cun-sheng. Microstructure evolution of spray deposited and as-cast 2195 Al−Li alloys during homogenization [J]. Journal of Materials Science & Technology, 2021, 82: 161−178.

[19] DENG Yun-lai, XU Jin-jun, CHEN Ji-qiang, GUO Xiao-bin. Effect of double-step homogenization treatments on the microstructure and mechanical properties of Al−Cu−Li−Zr alloy [J]. Materials Science and Engineering: A, 2020, 795: 139975.

[20] LIU Qi-bing, FAN Gen-lian, TAN Zhan-qiu, LI Zhi-qiang, ZHANG Di, WANG Jia, ZHANG Hao. Precipitation of Al_3Zr by two-step homogenization and its effect on the recrystallization and mechanical property in 2195 Al−Cu−Li alloys [J]. Materials Science and Engineering: A, 2021, 821: 141637.

[21] GUO You-jie, LI Jin-feng, LU Ding-ding, DENG San-xi, ZENG Guang-jun, MA Yun-long, YOU Wen, CHEN Yong-lai, ZHANG Xu-hu, ZHANG Rui-feng. Characterization of Al_3Zr precipitation via double-step homogenization and recrystallization behavior after subsequent deformation in 2195 Al−Li alloy [J]. Materials Characterization, 2021, 182: 111549.

[22] SENKOV O N, SHAGIEV M R, SENKOVA S V, MIRACLE D B. Precipitation of $Al_3(Sc,Zr)$ particles in an Al−Zn−Mg−Cu−Sc−Zr alloy during conventional solution

heat treatment and its effect on tensile properties [J]. Acta Materialia, 2008, 56: 3723−3738.

[23] LIU C L, AZIZI-ALIZAMINI H, PARSON N C, POOLE W J, DU Q. Microstructure evolution during homogenization of Al−Mg−Si−Mn−Fe alloys: Modelling and experimental results [J]. Transactions of Nonferrous Metals Society of China, 2017, 27: 747−753.

[24] DUMONT M, LEFEBVRE W, DOISNEAU-COTTIGNIES B, DESCHAMPS A. Characterisation of the composition and volume fraction of η' and η precipitates in an Al−Zn−Mg alloy by a combination of atom probe, small-angle X-ray scattering and transmission electron microscopy [J]. Acta Materialia, 2005, 53: 2881−2892.

[25] WANG Yong-xiao, ZHAO Guo-qun, XU Xiao, CHEN Xiao-xue, ZHANG Wen-dong. Microstructures and mechanical properties of spray deposited 2195 Al−Cu−Li alloy through thermo-mechanical processing [J]. Materials Science and Engineering: A, 2018, 727: 78−89.

[26] KIM J H, JEUN J H, CHUN H J, LEE Y R, YOO J T, YOON J H, LEE H S. Effect of precipitates on mechanical properties of AA2195 [J]. Journal of Alloys and Compounds, 2016, 669: 187−198.

[27] STEUWER A, DUMONT M, ALTENKIRCH J, BIROSCA S, DESCHAMPS A, PRANGNELL P B, WITHERS P J. A combined approach to microstructure mapping of an Al−Li AA2199 friction stir weld [J]. Acta Materialia, 2011, 59: 3002−3011.

[28] ENTRINGER J, REIMANN M, NORMAN A, DOS SANTOS J F. Influence of Cu/Li ratio on the microstructure evolution of bobbin-tool friction stir welded Al−Cu−Li alloys [J]. Journal of Materials Research and Technology, 2019, 8: 2031−2040.

[29] YU Xin-xiang, YIN Deng-feng, YU Zhi-ming, ZHANG Yi-ran, LI Shu-fei. Microstructure evolution of novel Al−Cu−Li−Ce alloys during homogenization [J]. Rare Metal Materials and Engineering, 2016, 45: 1687−1694.

[30] JIA Min, ZHENG Zi-qiao, GONG Zhu. Microstructure evolution of the 1469 Al−Cu−Li−Sc alloy during homogenization [J]. Journal of Alloys and Compounds, 2014, 614: 131−139.

[31] ZHANG Jin-shuo, ZHONG Xiao-xiang, ZHANG Liang, WU Guo-hua, LIU Wen-cai. Effect of heat treatments on microstructure and mechanical properties of sand cast Al−2Li−2Cu−0.5Mg−0.2Sc−0.2Zr alloy [J]. Transactions of Nonferrous Metals Society of China, 2022, 32: 411−423.

[32] MIKHAYLOVSKAYA A V, MOCHUGOVSKIY A G, LEVCHENKO V S, TABACHKOVA N Y U, MUFALO W, PORTNOY V K. Precipitation behavior of $L1_2$ Al_3Zr phase in Al−Mg−Zr alloy [J]. Materials Characterization, 2018, 139: 30−37.

[33] LI Ming, HUANG Yuan-chun, LIU Yu, WANG Xu, WANG Zhou. Effects of heat treatment before extrusion on dynamic recrystallization behavior, texture and mechanical properties of as-extruded Mg−Gd−Y−Zn−Zr alloy [J]. Materials Science and Engineering: A, 2022, 832: 142479.

[34] VARSCHAVSKY A, DONOSO E. The influence of particle shape on the non-isothermal kinetics of precipitate dissolution [J]. Thermochimica Acta, 1983, 69: 341−348.

[35] WHELAN M J. On the kinetics of precipitate dissolution [J]. Metal Science Journal, 1969, 3: 95−97.

[36] LIU Xiao-yan, PAN Qing-lin, FAN Xi, HE Yun-bin, LI Wen-bin, LIANG Wen-jie. Microstructural evolution of Al−Cu−Mg−Ag alloy during homogenization [J]. Journal of Alloys and Compounds, 2009, 484: 790−794.

[37] WANG Xiao-ying, JIE Wan-qi. Controlled melting process of off-eutectic alloy [J]. Acta Materialia, 2004, 52: 415−422.

[38] AARON H B, KOTLER G R. Second phase dissolution [J]. Metallurgical Transactions, 1971, 2: 393−408.

[39] ROBSON J D, PRANGNELL P B. Modelling Al_3Zr dispersoid precipitation in multicomponent aluminium alloys [J]. Materials Science and Engineering: A, 2003, 352: 240−250.

[40] KEITH E K, DAVID C D, DAVID N S. Precipitation evolution in Al−Zr and Al−Zr−Ti alloys during isothermal aging at 375−425 °C [J]. Acta Materialia, 2008, 56: 114−127.

[41] MOCHUGOVSKIY A G, MIKHAYLOVSKAYA A V, TABACHKOVA N Y, PORTNOY V K. The mechanism of $L1_2$ phase precipitation, microstructure and tensile properties of Al−Mg−Er−Zr alloy [J]. Materials Science and Engineering: A, 2019, 744: 195−205.

[42] MA Yu, ADDAD A, JI Gang, ZHANG Ming-xing, LEFEBVRE W, CHEN Zhe, JI V. Atomic-scale investigation of the interface precipitation in a TiB_2 nanoparticles reinforced Al–Zn–Mg–Cu matrix composite [J]. Acta Materialia, 2020, 185: 287−299.

[43] DING Li-peng, ZHAO Lv, WENG Yao-yao, SCHRYVERS D, LIU Qing, IDRISSI H. Atomic-scale investigation of the heterogeneous precipitation in the E ($Al_{18}Mg_3Cr_2$) dispersoid of 7075 aluminum alloy [J]. Journal of Alloys and Compounds, 2021, 851: 156890.

[44] LI Yong, LU Bing, YU Wei, FU Jin-yu, XU Guang-ming, WANG Zhao-dong. Two-stage homogenization of Al−Zn−Mg−Cu−Zr alloy processed by twin-roll casting to improve $L1_2$ Al_3Zr precipitation, recrystallization resistance, and performance [J]. Journal of Alloys and Compounds, 2021, 882:160789.

[45] KNIPLING K E, DUNAND D C, SEIDMAN D N. Criteria for developing castable, creep-resistant aluminum-based alloys—A review [J]. Ztschrift Fur Metallkunde, 2006, 97: 246−265.

[46] XIAO Tao, DENG Yun-lai, YE Ling-ying, LIN Hua-qiang, SHAN Chao-jun, QIAN Peng-wei. Effect of three-stage homogenization on mechanical properties and stress corrosion cracking of Al−Zn−Mg−Zr alloys [J]. Materials Science and Engineering: A, 2016, 675: 280−288.

[47] YUAN Zhi-peng, TU Yi-you, YUAN Ting, HUANG Yao-hua, ZHANG Yun-he. Effect of the interaction between Fe and Si on the precipitation behavior of dispersoids in Al−Mn alloys during homogenization [J]. Vacuum, 2021, 184: 109915.

[48] DOHERTY R D, HUGHES D A, HUMPHREYS F J,

JONAS J J, JENSEN D J, KASSNER M E, KING W E, MCNELLEY T R, MCQUEEN H J, ROLLETT A D. Current issues in recrystallization: A review [J]. Materials Science and Engineering: A, 1997, 238: 219−274.

[49] HUANG K E, LOGÉ R E. A review of dynamic recrystallization phenomena in metallic materials [J]. Materials & Design, 2016, 111: 548−574.

[50] HUANG Ke, MARTHINSEN K, ZHAO Qing-long, ROLAND E L. The double-edge effect of second-phase particles on the recrystallization behaviour and associated mechanical properties of metallic materials [J]. Progress in Materials Science, 2018, 92: 284−359.

均匀化处理对 2195 铝锂合金显微组织及再结晶行为的影响

付 绒[1]，黄元春[1,2,3]，刘 宇[3]，李 辉[1]，王志文[3]

1．中南大学 机电工程学院，长沙 410083；

2. 中南大学 高性能复杂制造国家重点实验室，长沙 410083；

3. 中南大学 轻合金研究院，长沙 410083

摘 要：采用扫描电镜、X 射线衍射、透射电镜及电子背散射衍射等方法研究均匀化处理过程中 2195 合金的显微组织演变和 Al_3Zr 析出相对再结晶行为的影响。结果表明，经均匀化处理后，铸态合金中严重的枝晶偏析得到有效消除，但其过程受到溶解速度较慢的 Al−Cu 相的限制。此外，与其他均匀化处理工艺(单级、双级和以 60 ℃/h 斜坡升温的均匀化处理)相比，在以 30 ℃/h 斜坡升温的均匀化处理条件下，样品(H30)中析出尺寸较细小且密度较大的 Al_3Zr 弥散相。Al_3Zr 弥散相的尺寸越小，密度越高，其具有的 Zener 钉扎阻力越强，可阻碍位错及(亚)晶界的移动。因此，在热压缩及后续固溶处理过程中 H30 样品表现出较强的再结晶抗力。该研究能为铸态 2195 铝合金热处理工艺参数的优化提供理论指导。

关键词：Al−Cu−Li 合金；均匀化；Al−Cu 相溶解；Al_3Zr 析出相；再结晶

(Edited by Wei-ping CHEN)